crystals

MDPI

Article

Crystal-Chemical Properties of Synthetic Almandine-Pyrope Solid Solution by X-Ray Single-Crystal Diffraction and Raman Spectroscopy

Yunqian Kuang [1,2,3], Jingui Xu [4], Bo Li [1,2], Zhilin Ye [1,2], Shijie Huang [1,2], Wei Chen [1,2,5], Dongzhou Zhang [4], Wenge Zhou [1,*] and Maining Ma [6,*]

1 Key Laboratory for High-Temperature and High-Pressure Study of the Earth's Interior, Institute of Geochemistry, Chinese Academy of Sciences, Guiyang 550081, China; kuangyunqian@126.com (Y.K.); fenberlee@163.com (B.L.); cugbyezhilin@163.com (Z.Y.); roberthuang1996@126.com (S.H.); chen123wei860701@163.com (W.C.)
2 University of Chinese Academy of Sciences, Beijing 100049, China
3 Bureau of Natural Resources and Planning of Yongzhou, Yongzhou 425000, China
4 Hawaii Institute of Geophysics and Planetology, School of Ocean and Earth Science and Technology, University of Hawaii at Manoa, Honolulu, HI 96822, USA; xujingui1990@126.com (J.X.); dzhang@hawaii.edu (D.Z.)
5 Guizhou Polytechnic of Construction, Guiyang 551400, China
6 Key Laboratory of Computational Geodynamics, College of Earth and Planetary Sciences, University of Chinese Academy of Sciences, Beijing 100049, China
* Correspondence: zhouwenge@vip.gyig.ac.cn (W.Z.); mamn@ucas.ac.cn (M.M.)

Received: 31 August 2019; Accepted: 17 October 2019; Published: 19 October 2019

Abstract: Crystal-chemical properties of synthetic Almandine-Pyrope (Alm-Pyr) solid solutions were investigated by X-ray single-crystal diffraction and Raman spectroscopy. Garnet solid solution with different compositions were synthesized from powder at 4.0 GPa and annealed at 1200 °C for 48 h by a multi-anvil pressure apparatus. Garnet crystals with different sizes (about 60–1000 μm) were obtained from synthesis. The results of X-ray single-crystal diffraction show that the unit cell constants decrease with increasing Pyr contents in the synthetic Alm-Pyr crystals due to the smaller ionic radius of Mg^{2+} in eightfold coordination than that of Fe^{2+}. The data exhibit obviously positive deviations from ideal mixing volumes across the Alm-Pyr join which may be caused by the distortion of the SiO_4 tetrahedron. Moreover, the significant decrease in the average M-O bond length and volume of the [MgO_8]/[FeO_8] dodecahedron with increasing Pyr contents are the most important factors to the decrease in the Alm-Pyr crystal unit cell constant and volume. On the other hand, selected bond distances (average <M-O>, <Al-O>, and <D-O> distances) have a linear correlation with the unit-cell parameter, but the <Si-O> distance has nonlinear correlation. With increasing the unit-cell parameter, the average <M-O> distance increases significantly, followed by the average <D-O> and <Al-O> distances. While the <Si-O> distance changes negligibly further confirming the conclusion that the significant decrease of the average M-O bond length of the [MgO_8]/[FeO_8] dodecahedron with increasing Pyr contents are the most important factors to the decrease in the Alm-Pyr crystal unit cell volume. In the Raman spectra collected for the Alm-Pyr solid solutions, Raman vibration mode assignments indicate that the Raman vibrational spectra change along the Alm-Pyr binary solution. The mode frequencies of Si-O stretching, Si-O bending, and the rotation of the SiO_4-tetrahedron (R(SiO_4)) decrease linearly, while the translational modes of the SiO_4-tetrahedron (T(SiO_4)) increase with increasing Alm contents.

Keywords: synthetic almandine-pyrope solid solution; crystal-chemical property; X-ray single-crystal diffraction; Raman spectroscopy

1. Introduction

Garnet is not only one of the most important mineral in the upper mantle [1], but also an important phase in metamorphic rocks [2]. Hence, garnet is stable over a wide range of pressures and temperatures in the Earth. In addition, garnet plays a prominent role in many geothermobarometers used to calculate the pressure and temperature of the mantle and metamorphic rock [3,4]. Therefore, the crystal-chemical properties concerning the elastic-strain, thermodynamic and trace-element substitution behavior of garnet are important for constraining the compositions, thermodynamic and physical properties of rocks in the middle-low crust and upper mantle.

The garnet group is a variety of nesosilicate minerals with an isolated group of [SiO_4] as its basic skeleton, including all garnets of essentially the same structure and chemically similar elements, and belongs to the cubic system and space group $Ia\bar{3}d$. The general formula for the garnet group is $X_3Y_2Z_3O_{12}$, where X, Y, and Z refer to dodecahedral, octahedral, and tetrahedral sites, respectively [5] (Figure 1). Generally, the X site is occupied by Mg^{2+}, Fe^{2+}, Mn^{2+}, Ca^{2+}, etc. The Y site is occupied by Al^{3+}, Fe^{3+}, Cr^{3+}, Ti^{4+}, etc. Si^{4+} and Al^{3+} occupy the Z site. The minerals of the garnet group are divided into two series, pyralspite and ugrandite, depending on the cation in the X site. If the X site of garnet is mainly occupied by Mg^{2+}, Fe^{2+}, and Mn^{2+}, it is pyralspite, while if the X site is mainly occupied by Ca^{2+}, it is ugrandite. However, most of garnet group samples in nature occur as multi-component solid solutions. For example, the pyrope (Pyr) component of garnet found in diamonds of peridotitic and eclogitic origin can be as high as about 79 mol.% and 43 mol.%, respectively, and the almandine (Alm) component is about 11 mol.% and 33 mol.%, respectively [6].

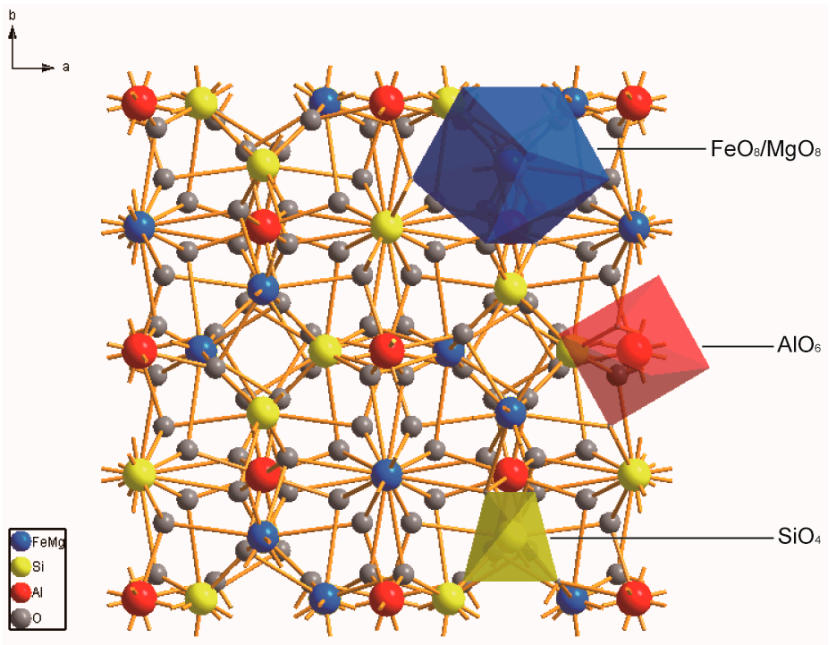

Figure 1. Crystal structure of garnet at ambient conditions.

The structure, elastic properties, and electrical conductivity of garnet end-members have been extensively studied, but detailed studies on structure by X-ray single-crystal diffraction and Raman spectroscopy of garnet solid solutions are limited. In particular, Raman spectroscopy studies have only focused on grossular-andradite join, pyrope-grossular join, and almandine-pyrope (Alm-Pyr) join [7–10]. To date, even in the most studied Alm-Pyr join, the structural properties of Alm-Pyr solid solution by the X-ray single-crystal diffraction are very limited, only several garnet compositions along the Alm-Pyr solid solution have been investigated by the X-ray single-crystal diffraction in details [11]. However, only when the strictly binary solid-solution compositions are available can we

fully understand how the natural garnet structure changes as a function of composition. Therefore, the crystal-chemical properties of the Alm-Pyr solid solution require further systematic research.

In this study, we firstly synthesize 11 garnet compositions along the Alm-Pyr solid solution at high pressure and high temperature. Then we select 10 garnets for X-ray single-crystal diffraction and 9 garnets for Raman spectroscopy studies. Finally, we discuss the effect of composition on the crystal-chemical properties along the Alm-Pyr binary.

2. Experiments

2.1. Crystal Synthesis

Eleven single crystals of Alm-Pyr garnet (Alm_{100}, Pyr_9Alm_{91}, $Pyr_{14}Alm_{86}$, $Pyr_{23}Alm_{76}$, $Pyr_{31}Alm_{68}$, $Pyr_{48}Alm_{52}$, $Pyr_{57}Alm_{43}$, $Pyr_{67}Alm_{32}$, $Pyr_{78}Alm_{22}$, $Pyr_{87}Alm_{12}$, and Pyr_{100}) used in this study were synthesized at high pressure and high temperature using a multi-anvil pressure apparatus (YJ-3000t) at the Institute of Geochemistry, Chinese Academy of Sciences, Guiyang, China. The sample assembles and synthesis process were similar to those used by Fan et al. (2017) and Xu et al. (2018) [12,13], and were briefly described here.

The starting materials used in the synthesizing experiments were stoichiometric amounts of high-purity magnesium oxide (MgO), aluminum oxide (Al_2O_3), silica (SiO_2), Iron (Fe), and Ferric oxide (Fe_2O_3). The mixture was grounded in acetone at an agate mortar for 3 h and then heated for more than 12 h at 200 °C in a muffle furnace to eliminate adsorbed water. Finally, the mixture was encapsulated in the platinum capsules with 1 weight percent (wt.%) of deionized water. The graphite tube was used as the heater and the pressure transmitting medium was pyrophyllite. All complete assemblies were heated for more than 10 h at 200 °C in a muffle furnace before being loaded into the apparatus.

The sample assembly was first compressed to 4.0 GPa for over 20 min by a multi-anvil pressure apparatus (YJ-3000t) and then heated to 1200 °C in 20 min. After a run duration of 48 h, the garnet crystals with different sizes (about 60–1000 μm) were obtained from the quenched run product.

2.2. Analysis Methods

The synthetic single garnet crystals were observed by the stereoscopic microscope.

The compositions of garnet crystals with sizes larger than ~100 μm were performed at the Institute of Geochemistry, Chinese Academy of Sciences, Guiyang, China with an electron microprobe analysis (EMPA, JEOL Hyperprobe JXA-8500F microscope), operating at a 15 kV accelerating voltage, 20 nA beam current, and a beam size of 10 μm.

The synchrotron X-ray single-crystal diffraction experiments at ambient condition were carried out with a six-circle diffractometer at 13-BM-C experimental station of the Advanced Photon Source, Argonne National Laboratory. The wavelength of the incident X-ray was 0.4340 Å, and the beam size was 12 μm × 18 μm. Diffraction images were acquired on Dectris Pilatus 1M detector and calibrated using the ambient LaB_6 as the diffraction standard [14]. Stepped φ rotation exposures were collected for the single-crystal sample of different components, with an exposure time of 1 s/deg. The φ-rotation (from −170° to 170°) axis was horizontal and perpendicular to the incident X-ray direction. The diffraction images were analyzed using the Bruker APEX3 software. Crystal structures were refined from the intensity data using the SHELXL software, facilitated by Olex 2 user interfaces [15,16]. Table S1 in the supplements shows the unit-cell parameters and details of the structural refinement of the samples.

Raman spectra in this study were collected with the Renishaw Raman spectrometer equipped with a Peltier-cooled charge-coupled device (CCD) detector. The laser exciting the sample was 532 nm in wavelength. The laser light was focused on samples by using the Leica microscope with a long-distance 20× objective to a beam size of about 2 μm diameter and the laser power was 2 mW. Each Raman spectrum was collected with a total exposure time of 300 s. Nine spectra were collected from different points on each garnet sample and measured Raman data from 100 cm^{-1} to 1200 cm^{-1}. We fitted the

Raman peaks and obtained peak parameters, Raman mode frequencies, and peak widths [full width at half-maximum (FWHM)] from these spectra.

3. Results and Discussion

3.1. Synthetic Garnet Crystal

The microphotographs of the synthetic Alm-Pyr crystals are shown in Figure 2 and Figure S1 in the supplements. The synthetic Alm-Pyr crystals are available in a variety of colors and optical characteristics. The color of the crystals gradually changes from colorless to orange and maroon with the increase of Alm contents in the Alm-Pyr crystals from 0 mol.% to 100 mol.%. In the meantime, the Alm-Pyr crystals also gradually vary from transparent to translucent, and finally to nearly opaque. The typical dimension of Alm-Pyr crystals with granular forms ranges from about 60 μm up to more than 1 mm with the increase of Alm contents (Figure 2).

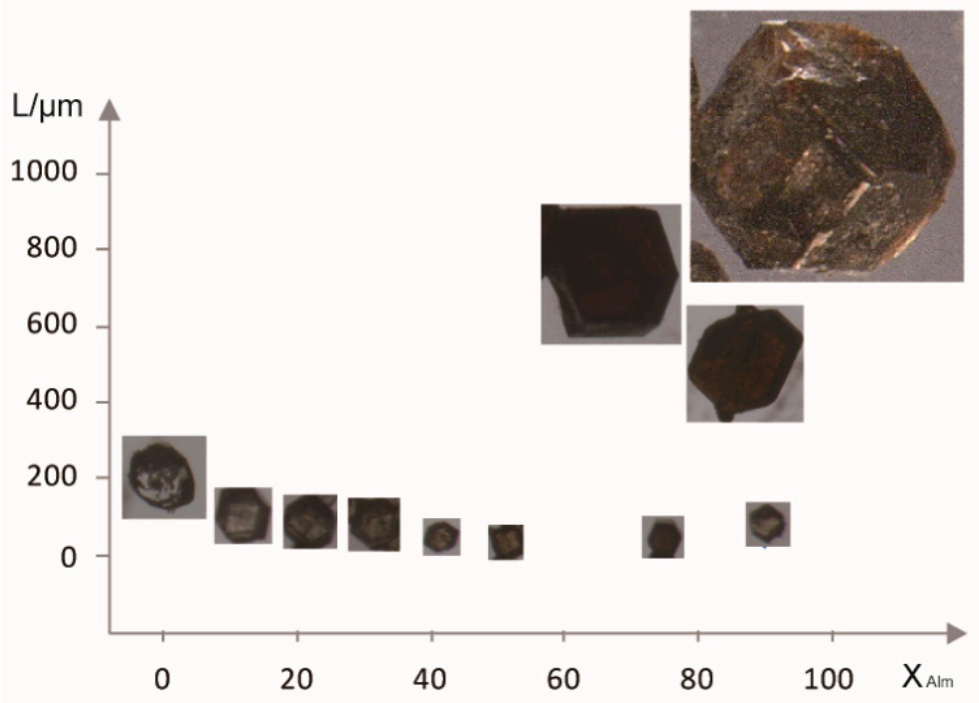

Figure 2. Typical microphotographs and dimensions of Alm-Pyr crystals synthesized in this study with increasing Alm contents.

The Alm-Pyr crystals have different grain size and morphology because the anisotropy of the growth fronts depends on the chemical composition [17] (Figure 2 and Figure S1). The microphotographs show that the largest grains are from sample Alm_{100} having a size of about 1000 μm. All samples have a combined form of rhombic dodecahedron {110} and tetragonal trisoctahedron {211}. Moreover, the faces of rhombic dodecahedron are more developed than those of tetragonal trisoctahedron (Figure S1).

3.2. Chemical Composition

All the 11 synthetic garnet compositions along the Alm-Pyr solid solution are given in Table 1. In addition, garnet crystal-chemical formulae were calculated according to the recommendations of Grew et al. (2013) [18] and also reported in Table 1.

Table 1. Garnet compositions along the pyrope–almandine solid solution.

Nominal Compositions	**Alm_{100}**	**$Pyr_{10}Alm_{90}$**	**$Pyr_{20}Alm_{80}$**	**$Pyr_{30}Alm_{70}$**	**$Pyr_{40}Alm_{60}$**	**$Pyr_{50}Alm_{50}$**	**$Pyr_{60}Alm_{40}$**	**$Pyr_{70}Alm_{30}$**	**$Pyr_{80}Alm_{20}$**	**$Pyr_{90}Alm_{10}$**	**Pyr_{100}**
EMPA Compositions	**Alm_{100}**	**$Pyr_{9}Alm_{91}$**	**$Pyr_{14}Alm_{86}$**	**$Pyr_{23}Alm_{76}$**	**$Pyr_{31}Alm_{68}$**	**$Pyr_{48}Alm_{52}$**	**$Pyr_{57}Alm_{43}$**	**$Pyr_{67}Alm_{32}$**	**$Pyr_{78}Alm_{22}$**	**$Pyr_{87}Alm_{12}$**	**Pyr_{100}**
wt.% of oxides											
SiO_2	35.76 (27)	36.83 (102)	36.37 (175)	36.26 (177)	38.33 (26)	38.88 (174)	40.11 (57)	41.21 (28)	42.68 (59)	43.28 (33)	43.34 (101)
TiO_2	1.58 (147)	0.90 (75)	1.20 (112)	0.87 (67)	1.34 (4)	0.05 (5)	0.18 (22)	0.55 (55)	0.01 (1)	0.20 (4)	0.11 (12)
Al_2O_3	19.81 (53)	20.10 (44)	20.25 (123)	19.96 (31)	21.15 (28)	21.57 (275)	22.23 (16)	22.72 (16)	22.20 (167)	24.13 (24)	24.36 (52)
FeO	46.04 (72)	43.09 (15)	40.32 (95)	38.33 (234)	33.94 (38)	23.37 (147)	22.17 (70)	17.13 (22)	11.98 (37)	6.83 (200)	0.05 (5)
MnO	0.01 (2)	0.01 (1)	0.01 (3)	0.01 (1)	0.02 (2)	0.01 (2)	0.02 (1)	0.01 (1)	0.01 (2)	0.00	0.01 (1)
MgO	0.01 (1)	2.30 (21)	3.56 (94)	6.59 (158)	8.74 (22)	12.11 (74)	16.65 (69)	19.95 (48)	23.68 (72)	26.91 (162)	30.66 (37)
CaO	0.02 (2)	0.03 (1)	0.05 (3)	0.07 (4)	0.10 (3)	0.07 (10)	0.09 (6)	0.14 (2)	0.15 (11)	0.11 (9)	0.01 (1)
Total	103.23 (20)	103.26 (124)	101.76 (440)	102.08 (12)	103.62 (57)	96.10 (328)	101.44 (80)	101.72 (63)	100.72 (77)	101.46 (64)	98.54 (191)
mol.% of garnets											
Pyrope	0.05 (4)	8.68 (69)	13.56 (334)	23.41 (545)	31.37 (76)	47.83 (260)	57.09 (187)	67.25 (42)	77.59 (108)	87.30 (406)	99.88 (11)
Spessartine	0.03 (2)	0.03 (3)	0.03 (6)	0.01 (1)	0.04 (4)	0.03 (5)	0.03 (3)	0.02 (1)	0.03 (3)	0.00	0.01 (3)
Grossular	0.04 (4)	0.08 (3)	0.13 (8)	0.18 (11)	0.26 (6)	0.20 (28)	0.23 (14)	0.34 (4)	0.36 (27)	0.26 (21)	0.02 (3)
Almandine	99.88 (8)	91.20 (69)	86.28 (333)	76.40 (532)	68.33 (83)	51.86 (286)	42.65 (172)	32.39 (45)	22.02 (104)	12.45 (384)	0.08 (9)
Total	100.00	100.00	100.00	100.00	100.00	100.00.00	100.00.00	100.00	100.00	100.00	100.00
Chemical formula	$Fe_{3.13}Al_{1.90}Ti_{0.1}Si_{2.91}O_{12}$	$(Fe_{2.88}Mg_{0.27})Al_{1.89}Ti_{0.05}Si_{2.94}O_{12}$	$(Fe_{2.71}Mg_{0.43})Al_{1.92}Ti_{0.07}Si_{2.92}O_{12}$	$(Fe_{2.55}Mg_{0.78})Al_{1.87}Ca_{0.01}Ti_{0.05}Si_{2.88}O_{12}$	$(Fe_{2.16}Mg_{0.99})Al_{1.9}Ca_{0.01}Ti_{0.08}Si_{2.92}O_{12}$	$(Fe_{1.52}Mg_{1.41})Al_{1.99}Ca_{0.01}Si_{3.04}O_{12}$	$(Fe_{1.36}Mg_{1.82})Al_{1.93}Ca_{0.01}Ti_{0.01}Si_{2.95}O_{12}$	$(Fe_{1.03}Mg_{2.13})Al_{1.92}Ca_{0.01}Ti_{0.03}Si_{2.95}O_{12}$	$(Fe_{0.71}Mg_{2.49})Al_{1.85}Ca_{0.01}Si_{3.01}O_{12}$	$(Fe_{0.39}Mg_{2.74})Al_{1.95}Ca_{0.01}Ti_{0.01}Si_{2.96}O_{12}$	$Mg_{3.12}Al_{1.96}Ti_{0.01}Si_{2.96}O_{12}$
Atom occupancy composition	**Alm_{100}**	**$Pyr_{11}Alm_{90}$**	**$Pyr_{16}Alm_{84}$**	**$Pyr_{28}Alm_{73}$**	**$Pyr_{41}Alm_{60}$**	**$Pyr_{45}Alm_{55}$**	**$Pyr_{52}Alm_{48}$**	**$Pyr_{67}Alm_{33}$**	**$Pyr_{75}Alm_{24}$**		**Pyr_{100}**

The EMPA results indicate that the synthesized garnet crystals consist almost entirely of Pyr and Alm, where the components of the Pyr and Alm are always greater than 99.6 mol.% and little grossular and spessartine (<0.4 mol.%) are also presented (Table 1). However, as shown in the Figure 3, except for the end members of Alm and Pyr garnets, the compositions of the other 9 synthetic Alm-Pyr crystals are obviously different from the nominal compositions of the starting material with Pyr contents less than those of nominal compositions (Figure 3). The result is basically consistent with occupancy factors obtained by structural refinement of the samples (Table 1 and Table S1). Expect for the samples with 10 mol.% and 40 mol.% Pyr in nominal composition and the end members of Alm and Pyr garnets, the measured compositions of the other 6 synthetic Alm-Pyr crystals are obviously different from the nominal compositions of the starting material with Pyr contents less than those of nominal compositions (Figure 3).

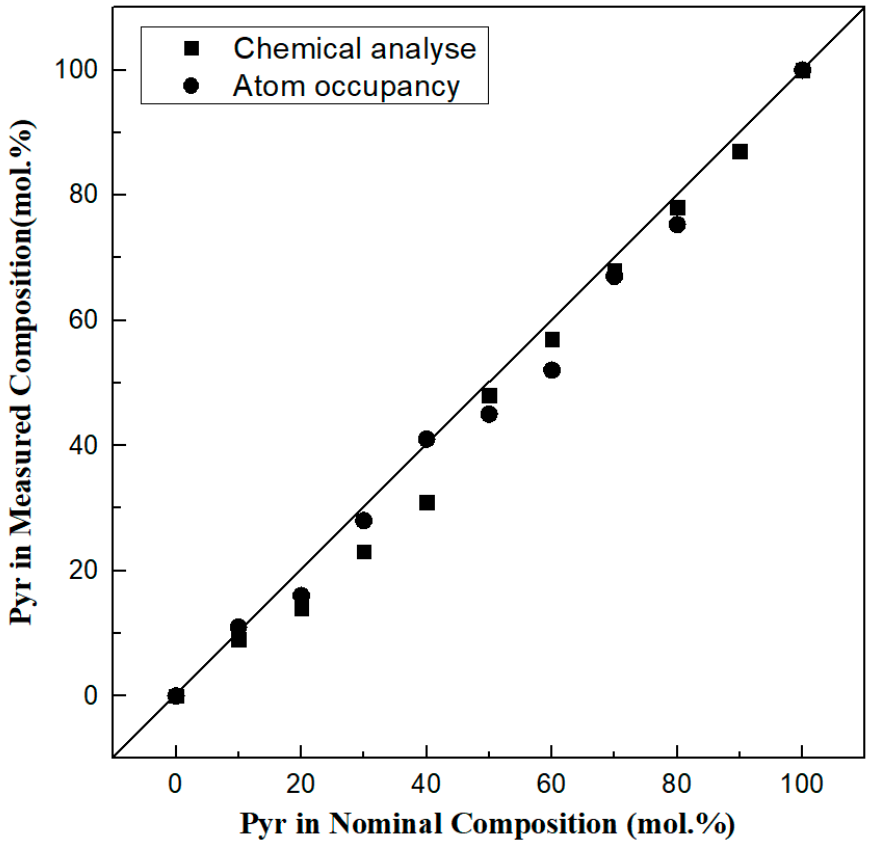

Figure 3. Relation between the measured composition and nominal composition for Alm-Pyr crystals.

3.3. Characteristics of Unit-Cell Parameters

The unit-cell parameters and the unit-cell volumes of the Alm-Pyr Crystals refined from the X-ray single-crystal diffraction are summarized in Table 2, along with the results of the previous studies for comparison [11,19,20]. Our results clearly showed that the unit cell constants decrease systematically with increasing Pyr contents in the synthetic Alm-Pyr crystals, due to the smaller ionic radius of Mg^{2+} in eightfold coordination (0.89 Å) than that of Fe^{2+} (0.92 Å) (Figure 4) [21].

The unit-cell measurements on the Alm-Pyr solid solutions exhibited considerably more scatter and positive deviations from ideal volumes of mixing across the Alm-Pyr join (Figure 4), which is contrary to the results obtained by the X-ray powder diffraction previously [22,23]. In theory, any solid solution deviates from the ideal solution properties to some extent. In the present case, the rotation of the SiO_4 tetrahedra is a possible cause of the positive deviations from ideal mixing volumes.

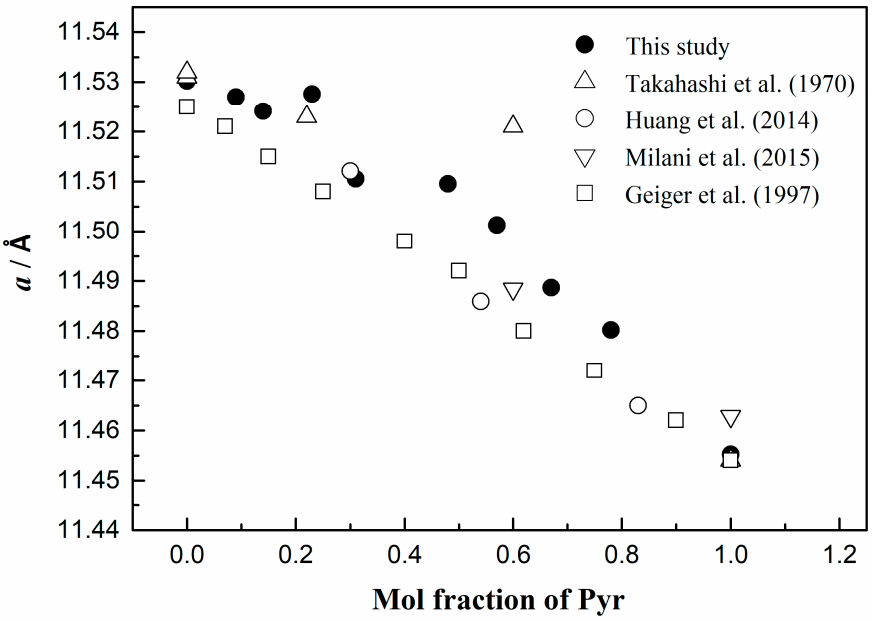

Figure 4. Unit cell constants versus the pyrope mol.% in Alm-Pyr crystals; The data of the previous studies are from the references of Takahashi et al. (1970) [20], Huang et al. (2014) [19], Milani et al. (2015) [11] and Geiger et al. (1997) [23].

Table 2. Unit-cell parameters and unit-volumes for almandine-pyrope crystals in this and previous studies [a].

Composition	Pry%	*a* (Å)	*V* (Å^3)	Reference
Alm_{100}	0	11.5320 (5)	1533.52	Takahashi et al. 1970 [20]
Alm_{100}	0	11.5330 (5)	1533.61	Takahashi et al. 1970 [20]
Alm_{100}	0	11.5303 (1)	1532.91 (4)	This study
Alm_{100}	0	11.530	1533.52 (10)	Milani et al. 2015 [11]
Alm_{100}	0	11.5291 (3)	1532.45	Geiger et al. 1997 [23]
Pyr_7Alm_{93}	7	11.5227 (2)	1529.90	Geiger et al. 1997 [23]
Pyr_9Alm_{91}	9	11.5270 (1)	1531.62 (4)	This study
$Pyr_{14}Alm_{86}$	14	11.5241 (3)	1530.46 (12)	This study
$Pyr_{15}Alm_{85}$	15	11.51570 (2)	1527.63	Geiger et al. 1997 [23]
$Pyr_{22}Alm_{72}$	22	11.5230 (5)	1530.02	Takahashi et al. 1970 [20]
$Pyr_{23}Alm_{76}$	23	11.5276 (2)	1531.85 (6)	This study
$Pyr_{25}Alm_{75}$	25	11.5105 (2)	1525.045	Geiger et al. 1997 [23]
$Pyr_{30}Alm_{70}$	30	11.5121 (3)	1526 (1)	Huang et al. 2014 [19]
$Pyr_{31}Alm_{68}$	31	11.5105 (1)	1525.06 (2)	This study
$Pyr_{40}Alm_{60}$	40	11.4995 (2)	1520.677	Geiger et al. 1997 [23]
$Pyr_{48}Alm_{52}$	48	11.5096 (1)	1524.67 (2)	This study
$Pyr_{50}Alm_{50}$	50	11.4925 (3)	1517.90	Geiger et al. 1997 [23]
$Pyr_{54}Alm_{46}$	54	11.4859 (1)	1515 (2)	Huang et al. 2014 [19]
$Pyr_{57}Alm_{43}$	57	11.5013 (4)	1521.39 (16)	This study
$Pyr_{60}Alm_{40}$	60	11.488	1516.32 (13)	Milani et al. 2015 [11]
$Pyr_{60}Alm_{31}$	60	11.521 (1)	1529.22	Takahashi et al. 1970 [20]
$Pyr_{62}Alm_{38}$	62	11.4830 (2)	1514.14	Geiger et al. 1997 [23]
$Pyr_{67}Alm_{32}$	67	11.4887 (3)	1516.40 (12)	This study
$Pyr_{75}Alm_{25}$	75	11.4737 (2)	1510.46	Geiger et al. 1997 [23]
$Pyr_{78}Alm_{22}$	78	11.4802 (1)	1513.04 (3)	This study
$Pyr_{83}Alm_{17}$	83	11.4650 (3)	1511 (1)	Huang et al. 2014 [19]
$Pyr_{90}Alm_{10}$	90	11.4612 (2)	1505.53	Geiger et al. 1997 [23]
Pyr_{100}	100	11.4552 (1)	1503.18 (4)	This study
Pyr_{100}	100	11.4555 (3)	1503.29	Geiger et al. 1997 [23]
Pyr_{100}	100	11.4540 (5)	1502.70	Takahashi et al. 1970 [20]
Pyr_{100}	100	11.463	1506.15 (16)	Milani et al. 2015 [11]

a. The data from Milani et al. (2015) [11] and this study were obtained by the single-crystal X-ray diffraction, while the other data from Takahashi et al. (1970) [20], Geiger et al. (1997) [23], and Huang et al. (2015) [19] were obtained by the powder X-ray diffraction.

Table 3 shows the bond lengths of average M-O (M is the cation in X site), Al-O, Si-O, D-O (D-O is the average distance from the four-coordinated O atom), and volumes of the $[MgO_8]$/$[FeO_8]$ dodecahedron, the $[AlO_6]$ octahedron, the $[SiO_4]$ tetrahedron with different compositions along the Alm-Pyr join. We found that the average Si-O bond length of the $[SiO_4]$ tetrahedron changes negligibly with increasing pyrope mol.%, while the variation of the volume is less than 0.014 $Å^3$. The variations of the average Al-O bond length and volume of $[AlO_6]$ octahedron with increasing pyrope mol.% are similar to those of the $[SiO_4]$ tetrahedron (Table 3). However, the behaviors of the average M-O bond length and volume with the increase in the pyrope molar fraction for the $[MgO_8]$/$[FeO_8]$ dodecahedron are quite different from those of the $[SiO_4]$ tetrahedron and $[AlO_6]$ octahedron. The average M-O bond length of the $[MgO_8]$/$[FeO_8]$ dodecahedron decreases significantly (Figure 5). Moreover, the decrease in the volume of the $[MgO_8]$/$[FeO_8]$ dodecahedron with the Pyr content is important for interpreting the decrease in the unit cell volume with the Pyr content, while the other factors, such as the distortion of the polyhedrons and the decrease in the $[SiO_4]$ tetrahedron and the $[AlO_6]$ octahedron volumes, may be secondary in importance.

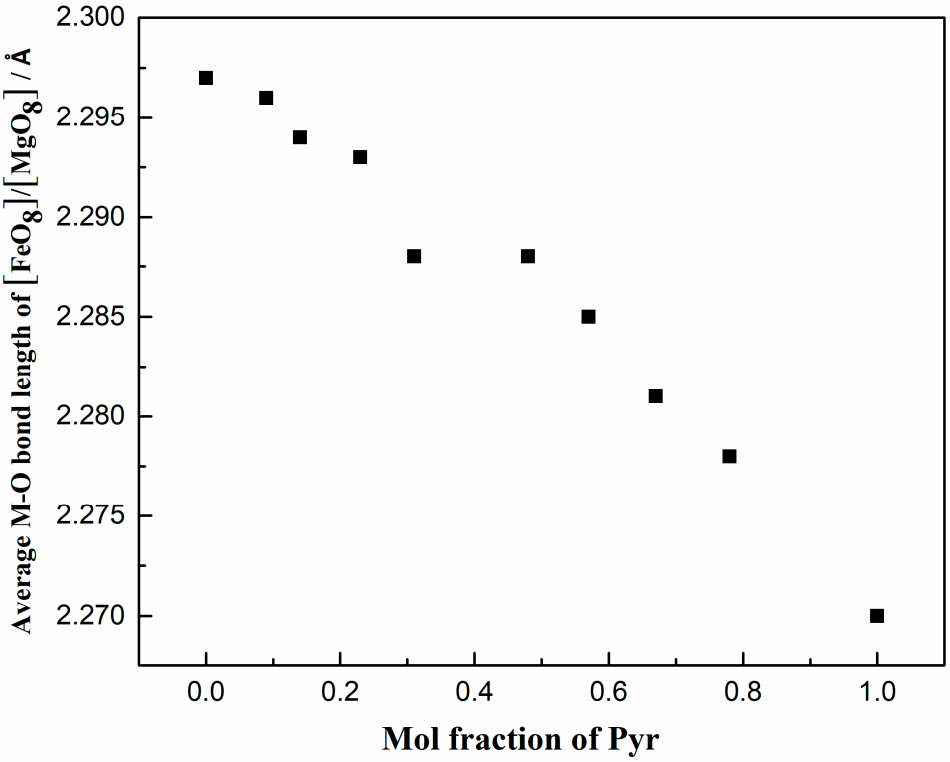

Figure 5. Average M-O bond length of $[MgO_8]$/$[FeO_8]$ dodecahedron versus the pyrope mol.%. M represents the Mg^{2+} or Fe^{2+}.

Table 3. Selected bond distances (Å) for almandine-pyrope garnet samples in this study.

Bond Distances	Alm_{100}	Pyr_9Alm_{91}	$Pyr_{14}Alm_{86}$	$Pyr_{23}Alm_{76}$	$Pyr_{31}Alm_{69}$	$Pyr_{48}Alm_{52}$	$Pyr_{57}Alm_{43}$	$Pyr_{67}Alm_{32}$	$Pyr_{78}Alm_{22}$	Pyr_{100}
M-O bond I length	2.2241 (9)	2.2218 (10)	2.2193 (12)	2.2203 (9)	2.2159 (9)	2.2153 (6)	2.2140 (9)	2.2088 (8)	2.2057 (7)	2.1993 (8)
M-O bond I length	2.3701 (10)	2.3704 (10)	2.3680 (12)	2.3662 (9)	2.3606 (9)	2.3598 (7)	2.3599 (9)	2.3532 (8)	2.3501 (7)	2.3400 (7)
Average <M-O>	2.2971 (10)	2.2962 (10)	2.2936 (12)	2.2933 (9)	2.2882 (9)	2.2876 (7)	2.2853 (9)	2.2810 (8)	2.2779 (7)	2.2779 (7)
$[FeO_8]/[MgO_8]$ volume	20.836	20.82	20.754	20.736	20.599	20.582	20.514	20.408	20.327	20.101
<Al-O>	1.8918 (10)	1.8907 (11)	1.8931 (13)	1.8954 (10)	1.8925 (10)	1.8913 (7)	1.8912 (10)	1.8901 (8)	1.8903 (7)	1.8860 (8)
$[AlO_6]$ volume	9.021	9.004	9.038	9.07	9.027	9.01	9.007	8.99	8.991	8.926
<Si-O>	1.6360 (10)	1.6360 (10)	1.6353 (13)	1.6360 (10)	1.6357 (10)	1.6370 (7)	1.6359 (10)	1.6349 (8)	1.6340 (7)	1.6350 (8)
$[SiO_4]$ volume	2.206	2.205	2.201	2.204	2.202	2.207	2.202	2.197	2.192	2.195
[a] <D-O>	2.029	2.02977	2.0289	2.0295	2.02615	2.02588	2.02442	2.02175	2.02003	2.0151
a (Å)	11.53025 (9)	11.52701 (11)	11.5241 (3)	11.52759 (16)	11.51055 (6)	11.50955 (6)	11.5013 (4)	11.4887 (3)	11.48023 (8)	11.45522 (10)

[a] <D-O> = {(Si-O) + (Al-O) + (M1-O) + (M2-O)}/4, which is the average distance from the four-coordinated O atom.

To eliminate the compositional variable, we also plot the bond distances versus the unit-cell parameter figures to the structural variations cross the Alm-Pyr solid solution. These figures show that the selected bond distances (average <M-O>, <Al-O>, and <D-O> distances) have a linear correlation with the unit-cell parameter, but the <Si-O> distance has nonlinear correlation which $R^2 = 0.284$. With increasing the unit-cell parameter, the average <M-O> distance increases significantly, followed by the average <D-O> and <Al-O> distances. However, the <Si-O> distance change negligibly (Table 3, Figure 6). Comparing our data with the previous study of Antao et al. (2014), we can find that our synthetic samples match those of natural samples quite well (Figure 6) [24]. The average <D-O> distance present optimal linear with the unit-cell parameter of all the data and other bond distances show more scatter than that for the average <D-O> distance, which may mean that satisfactory coordination of the O atom is most important for the garnet structure.

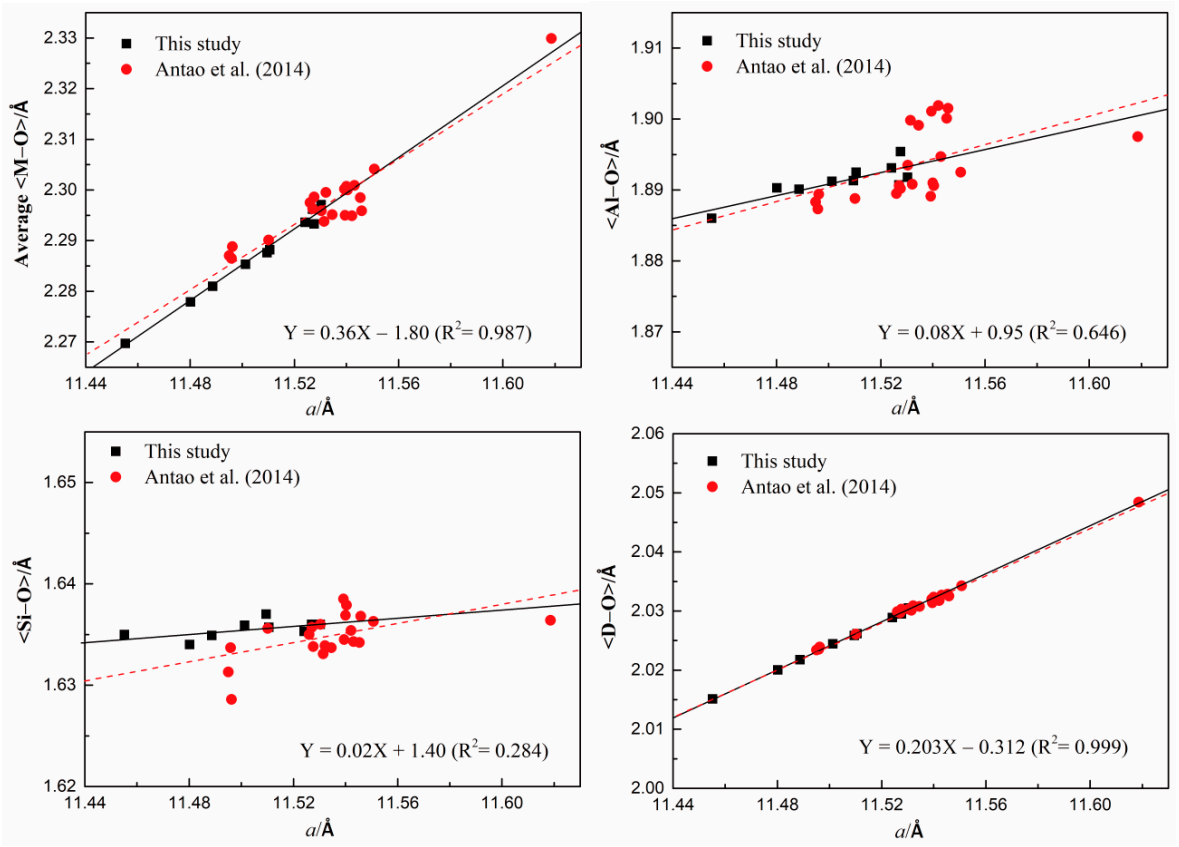

Figure 6. Structural variations across the Alm-Pyr solid solution series. Black square represents data and solid trend lines (black) are the linear fit to data from this study and their equations are given as inserts. Red circle represents data and dashed trend lines (red) are the linear fit to data from the reference of Antao et al. (2014) [24].

3.4. Excess Mixing Volume in Solid Solutions

As we can see, the unit-cell measurements on the Alm-Pyr solid solutions in our study exhibited considerably more scatter and positive deviations from ideal volumes of mixing across the Alm-Pyr join, which shows non-ideal mixing properties (Figure 7). However, our results should show near-ideal mixing properties because of the small difference in ionic radii of Mg^{2+} (0.89 Å) and Fe^{2+} (0.92 Å) in eightfold coordination [21]. There are lots of possible factors that could have caused excess volume such as dampness, synthesizing some unidentified phase and the distortion of the SiO_4 tetrahedra, etc. [9,25]. In this study, we think the cause might be the rotational orientation of the SiO_4 tetrahedra. As mentioned above, satisfactory coordination of the O atom is most important for the garnet structure and the relationship between the average <M-O> distance and the unit-cell parameter has more excellent linearity than the bond distances of <Al-O> and <Si-O>. Figure 8 shows the polyhedron structural variations across the Alm-Pyr solid solutions. The bond distances of <M-O> and <Al-O> vary linearly with their polyhedron volumes, but the <Si-O> distance exhibits more scatter and deviation from linearity (Table 3). Moreover, SiO_4 tetrahedra with the near-equal <Si-O> distance have different tetrahedra volumes, indicating the distortion of the SiO_4 tetrahedron. The possible reason for this is the substitution of Mg^{2+} and Fe^{2+} cations in the dodecahedral sites. The smaller ionic radius of Mg^{2+} in eightfold coordination (0.89 Å) than that of Fe^{2+} (0.92 Å) causes the shorter Mg-O bond length than Fe-O bond length, then causes the distortion of the SiO_4 tetrahedron. Therefore, we consider that the distortion of the SiO_4 tetrahedron is a possible reason leading to excess volume in this study.

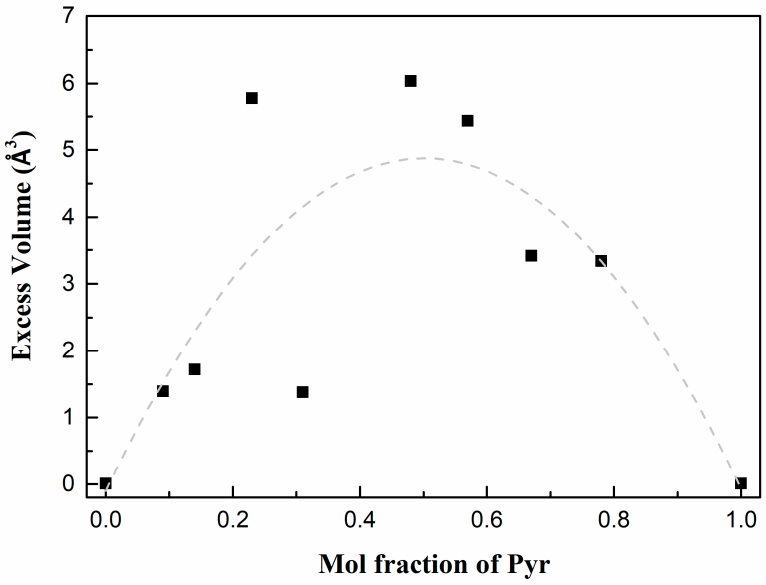

Figure 7. The excess volume versus the pyrope mol.%. Dashed lines (gray) is the polynomial fit to data.

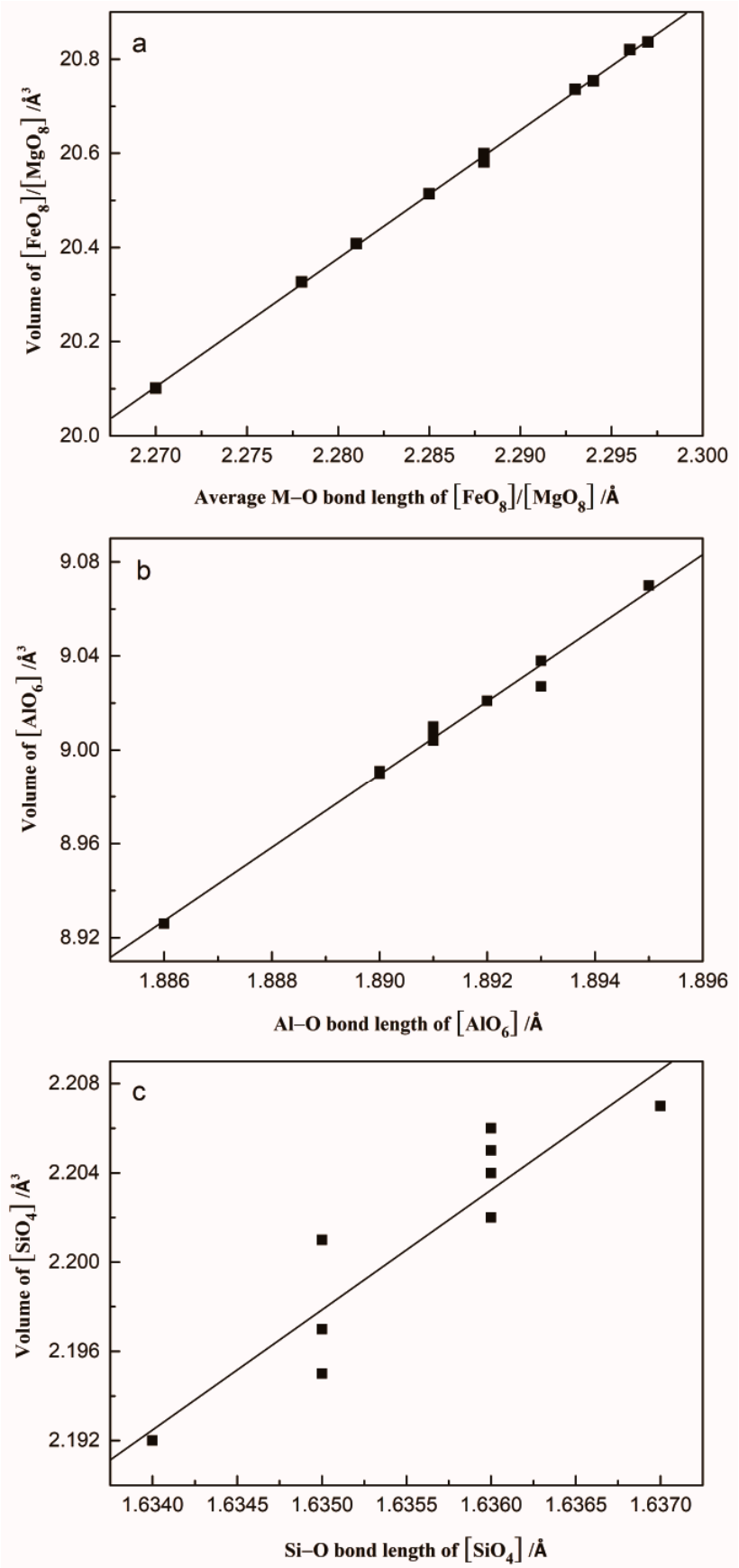

Figure 8. The polyhedron structural variations across the Alm-Pyr solid solutions. (**a**). The volume versus average M-O bond length of $[MgO_8]/[FeO_8]$ dodecahedron, M represents the Mg^{2+} or Fe^{2+}; (**b**). The volume versus Al-O bond length of $[AlO_6]$ octahedron; (**c**). The volume versus Si-O bond length of $[SiO_4]$ tetrahedron. Linear solid trend lines are fitted to data.

3.5. Characteristics of Raman Spectroscopy

Figure 9 shows the 9 Raman spectra collected from our Alm-Pyr solid solution series. Raman frequencies of peaks in these spectra and assigned Raman vibration modes are contained in Table 4. The peak positions in our study agree well with those of standard Raman spectra, and can be grouped into three distinct regions: low-frequency region between 167 cm^{-1} and 375 cm^{-1}; medium energy peaks (475–688 cm^{-1}); and high energy peaks (759–1060 cm^{-1}). The symmetry for the total vibrational modes of garnet calculated by factor group analysis (FGA) is given as follows [26–28]:

$$\Gamma_{total} = 3A_{1g} + 5A_{2g} + 8E_g + 14F_{1g} + 14F_{2g} + 5A_{1\mu} + 5A_{2\mu} + 10E_\mu + 18F_{1\mu} + 16F_{2\mu}$$

A total of 25 Raman active ($3A_{1g}$ + 8Eg + $14F_{2g}$) and 17 infrared-active ($17F_{1u}$) are expected. However, the observed vibrational modes are only 14 modes, which is less than the expected mode, and the peak around 330 cm^{-1}~350 cm^{-1} is mixed by J mode. The observed vibrational modes are grouped into three main regions (Figure 9). The highest frequency modes (A, B, C) are dominated by stretching motions of Si–O ((Si–O)str); the medium frequency modes at around 550 cm^{-1} (D, E, F, G, H) are dominated by bending motions of Si–O ((Si–O)bend); and the low-frequency modes are located at around 340 cm^{-1}, 210 cm^{-1}, and 168 cm^{-1}. The modes at around 340 cm^{-1} (I, J, K) are dominated by rotation motions of SiO_4 ($R(SiO_4)$). In addition, the mode at around 210 cm^{-1} (L) is due to translational motions of SiO_4 ($T(SiO_4)$) [29]. The mode at around 168 cm^{-1}(M) is due to the translation motion of Fe^{2+} [30], which appears in the samples with the Alm content higher than 52 mol.% (Figure 9).

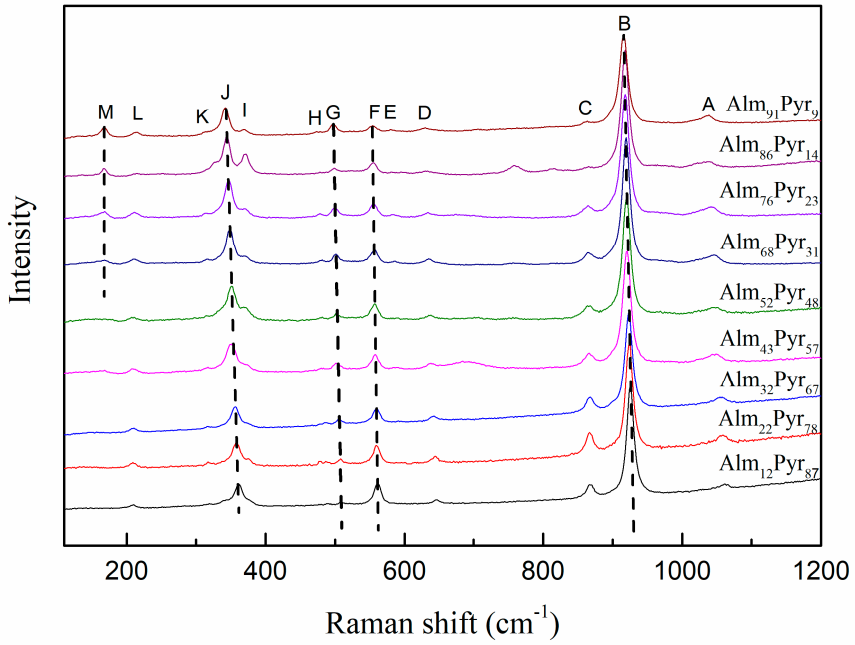

Figure 9. Raman spectra of garnets along Alm-Pyr binary. The marked M peaks represent the newly appearing Raman modes (translational modes of X-cations) for Alm-rich garnets.

Table 4. Raman mode frequencies (cm^{-1}) of garnet solid solution along almandine-pyrope binary recorded at ambient condition.

$Alm_{12}Pyr_{87}$	$Alm_{22}Pyr_{78}$	$Alm_{32}Pyr_{67}$	$Alm_{43}Pyr_{57}$	$Alm_{52}Pyr_{48}$	$Alm_{68}Pyr_{31}$	$Alm_{76}Pyr_{23}$	$Alm_{86}Pyr_{14}$	$Alm_{91}Pyr_{9}$	Assignment	Symmetry Species	Site Motion
1060	1057	1056	1045	1044	1041	1044	1035	1037	$(Si\text{-}O)_{str}$	F_{2g}	v_1 and v_3
924	924	923	920	920	919	918	916	916	$(Si\text{-}O)_{str}$	A_{1g}	
867	867	867	866	865	865	864			$(Si\text{-}O)_{str}$	F_{2g}	
							759 [b]			F_{2g}	
			688 [a]						$(Si\text{-}O)_{bend}$	F_{2g}	v_2 and v_4
644	644	642	638	637	635	634	633	630	$(Si\text{-}O)_{bend}$	F_{2g}	
			587		586	584		581	$(Si\text{-}O)_{bend}$	E_g	
560	560	559	558	557	556	555	555	556	$(Si\text{-}O)_{bend}$	A_{1g}	
507	508	506	503	503	501	500	499	500	$(Si\text{-}O)_{bend}$	F_{2g}	
		486	482	481	481	478	478	475	$(Si\text{-}O)_{bend}$	F_{2g}	
375	375	374	370	372	372	367	370	365	$R(SiO_4)$	F_{2g}	Rotation of SiO_4
358	358	356	350	351	349	347	344	342	$R(SiO_4)$	A_{1g}	
350	351	353	333			332	323	329	$R(SiO_4)$	F_{2g}	
318	318	318	317		315	314	314	316	$R(SiO_4)$	F_{2g}	
209	209	210	210	209	211	211	214	213	$T(SiO_4)$	E_g	Translation of SiO_4
						167	168	168	$T(X^{2+})$	F_{2g}	Translation of X cation

a. Modes observed by Du (2018) [9], b. Modes observed by Peng (1994) [31] and Theodore (2013) [32].

Figure 10 shows plots of different mode frequencies along Alm-Pyr binary. We can see that the Si-O stretching and Si-O bending modes frequencies decrease linearly with the Alm content. The A_{1g} spectra of the silicate garnets contain three modes around 350 cm^{-1}, 550 cm^{-1} and 900 cm^{-1}, and these modes have the maximum intensities. These selected A_{1g} mode and E_g mode frequencies of SiO_4 translation ($T(SiO_4)$) as functions of composition along Alm-Pyr binary are shown in detail in Figure 11. The $(Si\text{-}O)_{str}$ modes show stronger dependence on composition than the $(Si\text{-}O)_{bend}$. The Raman mode frequencies of the rotation of the SiO_4-tetrahedron ($R(SiO_4)$) decrease linearly with increasing Alm content, but the translational modes of the SiO_4-tetrahedron ($T(SiO_4)$) increase with increasing Alm content. The variation of the trends is attributed to a coupling between the vibrations of the translational modes of the SiO_4-tetrahedron and those of the translational modes of the X-site cations [9,29].

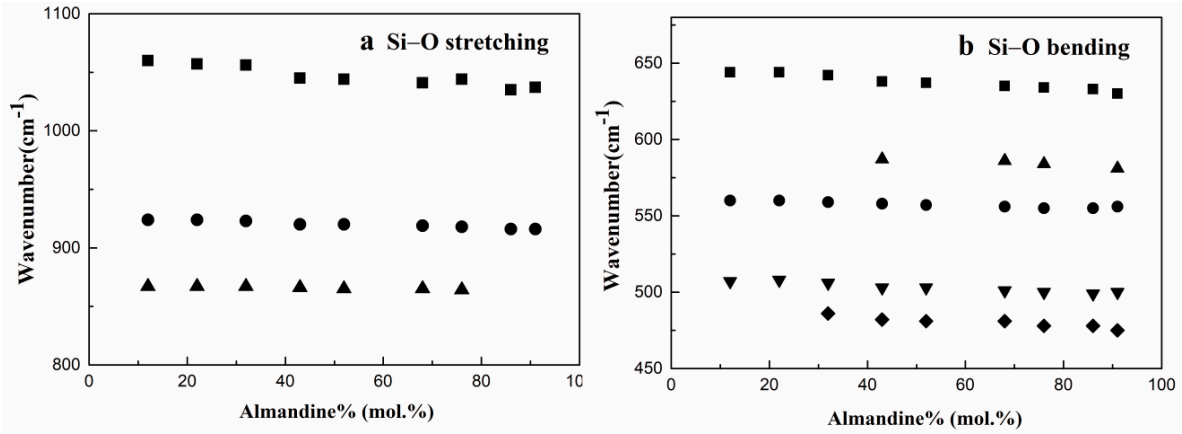

Figure 10. Composition dependence of frequencies of Raman modes corresponding to internal motions of SiO_4-tetrahedra: (**a**) Si–O stretching and (**b**) Si–O bending.

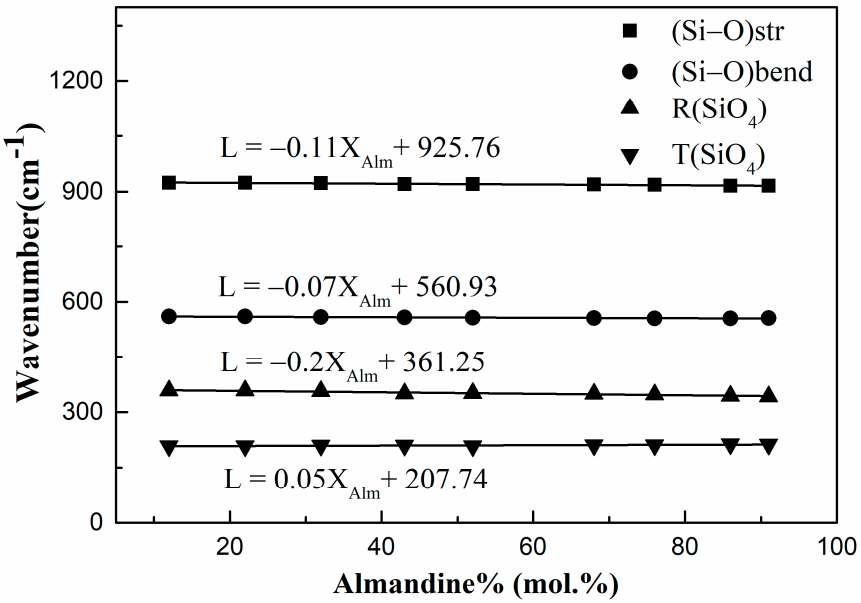

Figure 11. Selected Raman mode frequencies change with composition along Alm-Pyr binary. The solid lines are the linear fit results.

4. Conclusions

In summary, the crystal-chemical properties of the synthetic Alm-Pyr solid solution were carried out by X-ray single-crystal diffraction and Raman spectroscopy. Our results clearly show that the unit cell constants decrease with increasing Pyr contents (X_{Pyr}) in the synthetic Alm-Pyr crystals owing to the smaller ionic radius of Mg^{2+} in eightfold coordination (0.89 Å) than that of Fe^{2+} (0.92 Å). However, the data show considerably more scatter and positive deviations from ideal volumes of mixing across the Alm-Pyr join that may be caused by the distortion of the SiO_4 tetrahedron. Furthermore, the results of the refined crystal structures show that the average M-O bond length and the volume of the [MgO_8]/[FeO_8] dodecahedron decrease significantly. Moreover, the results also indicate that the variations of the average M-O bond length and the volume of the [MgO_8]/[FeO_8] dodecahedron with the Pyr content are the key factors concerning the variations of unit cell constant and volume of the Alm-Pyr solid solution. On the other hand, the average <M-O>, <Al-O>, and <D-O> bond distances have a linear correlation with the unit-cell parameter, while the <Si-O> distance has nonlinear correlation. Furthermore, the average <D-O> distance present optimal linear with the unit-cell parameter of all the data and other bond distances show more scatter than that for the average <D-O> distance, which may mean that satisfactory coordination of the O atom is most important for the garnet structure.

In addition, Raman mode frequencies of garnets along the Alm-Pyr solid solution series show the vibrational spectra change with the composition. The Si-O stretching, Si-O bending, and the rotation of the SiO_4-tetrahedron (R(SiO_4)) mode frequencies decrease linearly, but the translational mode frequencies of the SiO_4-tetrahedron (T(SiO_4)) increase with the Alm content. The variation of the trends is a result of the coupling between the vibration of the translational mode of the SiO_4-tetrahedron (R(SiO_4)) mode and that of the translational mode of the X-site cations.

Supplementary Materials: The following are available online at http://www.mdpi.com/2073-4352/9/10/541/s1, Figure S1: Microphotographs of the synthetic Alm-Pyr crystals, Table S1: Details of the structural refinement of synthesis single garnet crystals. CSD 1950879-1950888 contains the supplementary crystallographic data for this paper. These data can be obtained free of charge via http://www.ccdc.cam.ac.uk/conts/retrieving.html.

Author Contributions: Conceptualization, W.Z. and M.M.; Methodology, W.Z.; Funding acquisition, J.X. and M.M.; Investigation, Y.K., J.X., B.L., S.H., D.Z. and W.Z.; data analysis, Y.K.; Writing—original draft, Y.K.; Writing—review & editing, Y.K., J.X., Z.Y., W.C. and W.Z. All authors discussed the results.

Funding: This project was supported by the National Natural Science Foundation of China (Grant No. 41772043, 41802043 and 41674089), the Joint Research Fund in Huge Scientific Equipment (U1632112) under cooperative agreement between NSFC and CAS, the Chinese Academy of Sciences "Light of West China" Program (Dawei Fan, 2017; Jingui Xu, 2019), Youth Innovation Promotion Association CAS (Dawei Fan, 2018434), and Innovation and Entrepreneurship Funding of High-Level Overseas Talents of Guizhou Province (Dawei Fan, [2019] 10).

Acknowledgments: The synchrotron single-crystal X-ray diffraction experimental work was conducted at GeoSoilEnviroCARS (Sector 13), Partnership for Extreme Crystallography program (PX^2), Advanced Photon Source (APS), and Argonne National Laboratory. The authors thank Yuanyun Wen for her assistance during Raman spectroscopy experiments.

Conflicts of Interest: The authors declare no conflict of interest.

References

1. Ita, J.; Stixrude, L. Petrology, elasticity, and composition of the mantle transition zone. *J. Geophys. Res. Solid Earth* **1992**, *97*, 6849–6866. [CrossRef]
2. Fan, D.; Li, B.; Chen, W.; Xu, J.; Kuang, Y.; Ye, Z.; Zhou, W.; Xie, H. Research Progress of the Equation of State for Garnet Minerals. *Chin. J. High Press. Phys.* **2018**, *32*, 1–13.
3. Brey, G.P.; Kohler, T. Geothermobarometry in Four-phase Lherzolites II. New Thermobarometers, and Practical Assessment of Existing Thermobarometers. *J. Petrol.* **1990**, *31*, 1353–1378. [CrossRef]
4. Newton, R.C.; Perkins, D. Thermodynamic calibration of geobarometers based on the assemblages garnet-plagioclase-orthopyroxene (clinopyroxene)-quartz[1]. *Am. Mineral.* **1982**, *67*, 203–222.
5. Zhao, M. *Introduction to Minearlogy*, 2nd ed.; Geological Publishing House: Beijing, China, 2010; pp. 172–174.

6. Nestola, F.; Milani, S.; Angel, R.J.; Pasqual, D.; Geiger, C.A. Pressure-volume equation of state for pyrope-almandine solid solutions. In Proceedings of the EGU General Assembly Conference, Vienna, Austria, 7–12 April 2013.
7. Chopelas, A.; Savage, F. Single crystal raman spectroscopy and thermodynamics of garnet solid solutions I: Grossular-Andradite. In Proceedings of the American Geophysical Union Fall Meeting, San Francisco, CA, USA, 3–7 December 2012.
8. Sabeen, H.M.; Ramanujam, N.; Morton, A.C. The provenance of garnet: Constraints provided by studies of coastal sediments from southern India. *Sediment. Geol.* **2002**, *152*, 279–287. [CrossRef]
9. Du, W.; Han, B.; Clark, S.M.; Wang, Y.; Liu, X. Raman spectroscopic study of synthetic pyrope–grossular garnets: Structural implications. *Phys. Chem. Miner.* **2018**, *45*, 197–209. [CrossRef]
10. Savage, F.B.; Chopelas, A. Single Crystal Raman Spectroscopy and Thermodynamics of Garnet Solid Solutions II: Pyrope-Almandine Binary. In Proceedings of the American Geophysical Union Fall Meeting, San Francisco, CA, USA, 8–12 December 2003.
11. Milani, S.; Nestola, F.; Alvaro, M.; Pasqual, D.; Mazzucchelli, M.L.; Domeneghetti, M.C.; Geiger, C.A. Diamond–garnet geobarometry: The role of garnet compressibility and expansivity. *Lithos* **2015**, *227*, 140–147. [CrossRef]
12. Xu, J.; Zhang, D.; Fan, D.; Zhang, J.S.; Hu, Y.; Guo, X.; Dera, P.; Zhou, W. Phase Transitions in Orthoenstatite and Subduction Zone Dynamics: Effects of Water and Transition Metal Ions. *J. Geophys. Res. Solid Earth* **2018**, *123*, 2723–2737. [CrossRef]
13. Fan, D.; Chang, L.; Xu, J.; Yan, B.; Yang, B.; Chen, J. Effects of water on P-V-T equation of state of pyrope. *Phys. Earth Planet. Inter.* **2017**, *267*, 9–18. [CrossRef]
14. Zhang, D.; Dera, P.K.; Eng, P.J.; Stubbs, J.E.; Zhang, J.S.; Prakapenka, V.B.; Rivers, M.L. High Pressure Single Crystal Diffraction at PX^2. *J. Vis. Exp.* **2017**, *119*, e54660. [CrossRef]
15. Sheldrick, G.M. A short history of SHELX. *Acta Crystallogr. Sect. A* **2008**, *64*, 112–122. [CrossRef] [PubMed]
16. Dolomanov, O.V.; Bourhis, L.J.; Gildea, R.J.; Howard, J.A.K.; Puschmann, H. OLEX2: A complete structure solution, refinement and analysis program. *J. Appl. Crystallogr.* **2010**, *42*, 339–341. [CrossRef]
17. Cherepanova, T.A.; Bennema, P.; Yanson, Y.A.; Vogels, L.J.P.; Cherepanova, T.A.; Bennema, P.; Yanson, Y.A.; Vogels, L.J.P. Morphology of synthetic and natural garnets: Theory and observations. *J. Cryst. Growth* **1992**, *121*, 17–32. [CrossRef]
18. Grew, E.S.; Locock, A.J.; Mills, S.J.; Galuskina, I.O.; Galuskin, E.V.; Hålenius, U. Nomenclature of the garnet supergroup. *Am. Mineral.* **2013**, *98*, 785–811. [CrossRef]
19. Shu, H.; Chen, J. Equation of state of pyrope–almandine solid solution measured using a diamond anvil cell and in situ synchrotron X-ray diffraction. *Phys. Earth Planet. Inter.* **2014**, *228*, 88–91.
20. Takahashi, T.; Liu, L.G. Compression of Ferromagnesian Garnets and the Effect of solid solutions on the Bulk Modulus. *J. Geophys. Res.* **1970**, *75*, 5757–5766. [CrossRef]
21. Shannon, R.D. Revised effective ionic radii and systematic studies of interatomic distances in halides and chalcogenides. *Acta Crystallogr.* **1976**, *32*, 751–767. [CrossRef]
22. Geiger, C.A.; Newton, R.C.; Kleppa, O.J. Enthalpy of mixing of synthetic almandine-grossular and almandine-pyrope garnets from high-temperature solution calorimetry. *Geochimica Et Cosmochimica Acta* **1987**, *51*, 1755–1763. [CrossRef]
23. Geiger, C.A.; Feenstra, A. Molar volumes of mixing of almandine-pyrope and almandine-spessartine garnets and the crystal chemistry and thermodynamic-mixing properties of the aluminosilicate garnets. *Am. Mineral.* **1997**, *82*, 571–581. [CrossRef]
24. Antao, S.; Zaman, M.; Suarez Nieto, N.; Gontijo, V.; Marr, R. Structural variations in pyrope-almandine solid solutions. *Adv. X-Ray Anal.* **2014**, *58*, 90–107.
25. Du, W.; Clark, S.M.; Walker, D. Excess mixing volume, microstrain, and stability of pyrope-grossular garnets. *Am. Mineral.* **2016**, *101*, 193–204. [CrossRef]
26. Koningstein, J.A.; Mortensen, O.S. Electronic Raman Spectra. III. Absolute Cross Sections for Electronic Raman and Rayleigh Scattering. *Phys. Rev.* **1968**, *168*, 75–77. [CrossRef]
27. Moore, R.K.; White, W.B.; Long, T.V. Vibrational spectra of the common silicates: I. The garnets. *Am. Mineral.* **1971**, *56*, 54–71.
28. Fateley, W.G.; Mcdevitt, N.T.; Bentley, F.F. Infrared and Raman Selection Rules for Lattice Vibrations: The Correlation Method. *Appl. Spectrosc.* **1971**, *25*, 155–173. [CrossRef]

29. Kolesov, B.A.; Geiger, C.A. Raman spectra of silicate garnets. *Phys. Chem. Miner.* **1998**, *25*, 142–151. [CrossRef]
30. Sibi, N.; Subodh, G. Structural and Microstructural Correlations of Physical Properties in Natural Almandine-Pyrope Solid Solution: $Al_{70}Py_{29}$. *J. Electron. Mater.* **2017**, *46*, 1–10. [CrossRef]
31. Mingsheng, P.; Mao, H.K.; Dien, L.; Chao, E.C.T. Raman spectroscopy of garnet-group minerals. *Chin. J. Geochem.* **1994**, *13*, 176–183. [CrossRef]
32. Ganetsos, T.; Katsaros, T.; Vandenabeele, P.; Greiff, S.; Hartmann, S. Raman spectroscopy as a tool for garnet analysis and investigation on samples from different sources. *Int. J. Mater. Chem.* **2013**, *3*, 5–9.